Composites of BiVO$_4$ and g-C$_3$N$_4$: Synthesis, Properties and Photocatalytic Decomposition of Azo Dye AO7 and Nitrous Oxide

Petr Praus[1,2] · Jaroslav Lang[2] · Alexandr Martaus[2] · Ladislav Svoboda[1,2] · Vlastimil Matějka[1,2] · Martin Kormunda[3] · Marcel Šihor[2] · Martin Reli[2] · Kamila Kočí[2]

Abstract

The composites of BiVO$_4$ and g-C$_3$N$_4$ (BiVO$_4$/g-C$_3$N$_4$) were synthesised by the calcination of a mixture of monoclinic BiVO$_4$ and bulk g-C$_3$N$_4$ at 300 °C for 4 h. Both components were previously prepared by the precipitation of Bi(NO$_3$)$_3$ with NH$_4$VO$_3$ and annealing of melamine. X-ray photoelectron spectroscopy (XPS) identified the presence of C–O and C=O bonds as well as metal nitrides which confirmed the formation of a heterojunction between BiVO$_4$ and g-C$_3$N$_4$. The heterojunction was also indicated by UV–Vis diffuse reflectance (DRS) and photoluminescence (PL) spectroscopy. The band gap energies were determined at 2.42–2.46 eV of BiVO$_4$ and 2.75–2.82 eV of bulk g-C$_3$N$_4$. The specific surface area was 23–28 m^2 g^{-1} of the composites and 6 m^2 g^{-1} and 35 m^2 g^{-1} of pure BiVO$_4$ and g-C$_3$N$_4$, respectively. The photocatalytic activity of the composites was investigated by the decomposition of Acid Orange 7 (AO7) and nitrous oxide. In case of AO7, the BiVO$_4$/g-C$_3$N$_4$ (1:3) composite was the most active one and the main role in the reaction was played by photoinduced holes forming hydroxyl radicals. At the decomposition of N$_2$O, the most important species were the photoinduced electrons and the BiVO$_4$/g-C$_3$N$_4$ (1:1) composite was the most active photocatalyst.

Keywords BiVO$_4$ · G-C$_3$N$_4$ · Composites · Heterojunction · Photocatalysis

1 Introduction

Graphitic carbon nitride (g-C$_3$N$_4$) has attracted attention of many researchers from all over the world as a metal-free polymeric semiconducting material. Although, g-C$_3$N$_4$ was already synthetized by Liebig in 1834 and its properties were studied later, e.g. [1, 2], an immense interest of this material has started after a paper published by Wang et al. [3] about a photocatalytic water splitting under visible light. G-C$_3$N$_4$ has diamond-like properties, such as thermal, chemical and photochemical stability, due to tri-s-triazine (heptazine) (C$_6$N$_7$)-based building blocks and strong covalent bonds between carbon and nitrogen atoms [2]. G-C$_3$N$_4$ has been synthetized by the thermal condensation of nitrogen-rich precursors, such as cyanamide, dicyandiamide, melamine and so forth [4]. An interesting feature of g-C$_3$N$_4$ is its band gap energy of 2.7 eV which makes it possible working under visible light [5–7]. However, its photocatalytic applications are limited by a fast recombination of photoinduced electrons and holes. It can be overcome by doping of g-C$_3$N$_4$ structures with metals and non-metals [7, 8] and coupling with metal [9] and semiconductor nanoparticles forming heterojunction photocatalysts [6, 10–15].

Recently, we studied some composites of g-C$_3$N$_4$ with semiconductor nanoparticles, such as TiO$_2$ [16, 17], WO$_3$ [18, 19] and SnO$_2$ [20]. The composites of g-C$_3$N$_4$ with BiVO$_4$ particles were studied by several authors [21–24]. BiVO$_4$ exists in monoclinic, tetragonal and orthorhombic modifications. Monoclinic BiVO$_4$ is able to absorb visible light due to the band gap of 2.4 eV in contrast to tetragonal

✉ Petr Praus
petr.praus@vsb.cz

[1] Department of Chemistry, VŠB-Technical University of Ostrava, 17. listopadu 15/2172, 708 33 Ostrava, Czech Republic

[2] Institute of Environmental Technology, VŠB-Technical University of Ostrava, 17. listopadu 15/2172, 708 33 Ostrava, Czech Republic

[3] Faculty of Science, J. E. Purkyně University, České Mládeže 8, 400 96 Ústí nad Labem, Czech Republic

one with the band gap of 2.9 eV [25]. $BiVO_4$ has been investigated due to its low toxicity, photocatalytic [26, 27] and coloristic properties [28, 29]. $BiVO_4$ can be prepared by several methods, such as a hydrothermal [26, 28–30], mechanochemical [25], ultrasonic [31] and surfactant-assisted precipitation [32, 33] and an ultrasonic spray pyrolysis [34]. Graphitic carbon nitride as well as its heterostructures with other semiconductors has been tested for the decomposition of risky environmental pollutants in gas and liquid phase.

Nitrous oxide is one of compounds depleting the stratospheric ozone layer and also strongly contributing to the greenhouse effect. The most important sources of N_2O are agriculture (fertilized soils), fossil fuels combustion, biomass burning, chemical industry, the production of nitric and adipic acids, and all combustion processes including emissions from car engines. The direct decomposition of N_2O to nitrogen and oxygen could be a suitable for its removal but from a thermodynamic point of view it is spin-forbidden with a high activation energy and feasible at a temperature about 1000 K [35]. The photocatalytic decomposition of N_2O using appropriate photocatalysts is an alternative way which can be performed at ambient temperatures and atmospheric pressure [36].

Besides gaseous pollutants such as N_2O there is a significant amount of organic pollutants present in waters, for instance, biocides, pharmaceuticals, dyes etc. [37]. Photocatalysis is also capable to oxidatively decompose them due to high oxidation potentials of photoinduced holes. The photocatalytic decomposition of synthetic dyes, which are an important source of water contamination coming mainly from textile industry, has been intensively studied [38].

The aim of this paper was to synthetize some composites of $BiVO_4$ and g-C_3N_4 and to examine their physico-chemical properties including the photocatalytic activity. They are able to absorb visible light and, therefore, have been investigated in various technical disciplines. In this work, $BiVO_4$/g-C_3N_4 composites were obtained by calcination of the mixtures of both pure components at 300 °C and resulting materials were characterized by common instrumental methods. Their photocatalytic properties were tested by the decomposition of azo-dye Acid Orange 7 [39] and nitrous oxide.

2 Experimental

2.1 Chemicals

All the chemicals used were of analytical reagent grade. Melamine was purchased from Sigma-Aldrich (USA), NH_4VO_3, citric and nitric acids and 1,4-benzoquinone (1,4-BQ) were purchased from Lach-Ner (Czech Republic), $Bi(NO_3)_3$ 5 H_2O was purchased from Penta (Czech Republic), triethanolamine (TEOA) and tertial butanol (t-BuOH) from Lachema (Czech Republic). Azo-dye Acide Orange 7 was purchased from Synthesia (Czech Republic).

Water deionized by reverse osmosis (Aqua Osmotic, Czech Republic) was used for preparation of all solutions.

2.2 Preparation of g-C_3N_4

Melamine was heated in a ceramic crucible air in a muffle furnace. The heating temperature was gradually elevated with the heating rate of 15 °C min^{-1} at the final temperature of 620 °C and kept for 1 h [4]. The resulting product was ground into powder and store in a closed vessel at a laboratory temperature.

2.3 Preparation of $BiVO_4$

$BiVO_4$ was prepared by a sol–gel method [40]: $Bi(NO_3)_3$ 5 H_2O was dissolved in 2 mol l^{-1} HNO_3 and precipitated with NH_4VO_3 in the presence of citric acid. The resulting $BiVO_4$ was dried at 110 °C overnight and consequently heated at 500 °C for 5 h in a muffle furnace. The resulting product was ground into powder stored in a closed vessel at the laboratory temperature.

2.4 Preparation of $BiVO_4$/g-C_3N_4 Composites

The powders of $BiVO_4$ and g-C_3N_4 were mixed in mass portions of 1:1 and 1:3 and calcined at 300 °C for 4 h [40]. Together with the composites both pure components were heated in the same manner. The calcination products were ground into powder and stored in closed vessels at the laboratory temperature. The mass loss caused by heating of the materials was checked by their weighting after cooling; a weight loss of 0.06–0.70% was found. The composites were labelled as $BiVO_4$/g-C_3N_4 (1:1) and $BiVO_4$/g-C_3N_4 (1:3) according to the portion of both components. The content of Bi in the composites was determined by an atomic absorption spectrometer ContraAA 700 (Analytik Jena AG, Germany).

2.5 X-Ray Diffraction

The phase composition and microstructural properties of the prepared materials were determined using X-ray powder diffraction (XRD) technique. XRD patterns were obtained using a Rigaku SmartLab diffractometer (Rigaku, Japan) with a detector D/teX Ultra 250. A source of X-ray irradiation was a Co tube (CoKα, λ_1 = 0.178892 nm, λ_2 = 0.179278 nm) operated at 40 kV and 40 mA. Incident and diffracted beam optics were equipped with 5° Soller slits; incident slits were set up to irradiate area of a sample 10 × 10 mm (automatic divergence slits) constantly. Slits

on a diffracted beam were set up to a fixed value of 8 and 14 mm. The samples rotated (30 rpm) during measurements to eliminate preferred orientation effect. The XRD patterns were collected in a 2θ range of 5°–90° with a step size of 0.01° and speed 0.5°/min. The XRD patterns were evaluated using a PDXL 2 software (version 2.4.2.0) and compared with a database PDF-2, release 2015 and were analysed using the LeBail method to refine the lattice parameters of bismuth vanadate. Background of the XRD patterns was determined using the B-Spline function. Peak shapes were modelled with the pseudo-Voigt function accounting for a peak asymmetry due to axial divergence.

The crystallite size L was calculated according to Scherrer's equation for broadening $B(2\theta)$ (in radians) at a half maximum intensity (FWHM) of a diffraction peak as

$$B(2\Theta) = \frac{K\lambda}{L\cos\Theta} \tag{1}$$

where λ is the wavelength of X-rays, θ is Bragg´s angle and K is the constant equal to 0.94 for cube or 0.89 for spherical crystallites. In this study K was rounded to 0.9.

2.6 Fourier Transform Infrared Spectrometry

Fourier transform infrared (FTIR) spectroscopy was performed with a FT-IR spectrometer Nexus 470 (ThermoScientific, USA) equipped with a DTGS detector using the KBr pellet technique. The spectra were recorded in the region of 4000–400 cm^{-1} with a resolution of 4 cm^{-1} (64 scans; the Happ-Genzel apodization).

2.7 Raman Spectrometry

Raman spectra were recorded using a dispersive Raman spectrometer DXR SmartRaman (ThermoScientific, USA) with a CCD detector. A 180° degree sampling was used as a measurement technique of the Raman spectroscopy. The measurement parameters were performed in the spectral region of 1800–50 cm^{-1} with a excitation laser 780 nm, a grating of 400 lines mm^{-1} and a aperture of 50 μm (exposure time 1 s, the number of exposures was 1000). The spectra were treated with fluorescence correction (6th order).

2.8 XPS Spectrometry

X-ray photoelectron spectra were recorded using a Phoibos 100 (SPECS) hemispherical analyser operated in the FAT mode. The spectral line AlK_α of SPEXS XR50 was used to study a surface chemistry. High-resolution spectra for pass energy of 10 eV were utilized for quantification, and survey spectra were recorded at 40 eV for qualitative analyses. The sample composition was calculated from selected high-resolution spectra and corresponding RSF from the CasaXPS

library. The C–C component of the C 1s peak was set to a binding energy of 284.5 eV.

2.9 UV–Vis Diffuse Reflectance Spectrometry

UV–Vis DRS spectra were recorded with a Shimadzu UV-2600 (IRS-2600Plus) spectrophotometer at the room temperature in the range of 220–1400 nm. Reflectance was re-calculated to absorbance using Schuster-Kubelka-Munk's equation as follows

$$F(R_\infty) = \frac{(1 - R_\infty)^2}{2R_\infty} \tag{2}$$

where R_∞ is the diffuse reflectance from a semi-infinite layer. These DRS spectra were transformed to the dependencies of $(F(R_\infty)h\nu)^2$ on $h\nu$ in order for us to obtain band gap energies of the prepared materials.

2.10 Photoluminescence Spectroscopy

Photoluminescence spectra were recorded by a spectrometer FLSP920 Series (Edinburgh Instruments, Ltd.) in the range from 390 to 640 nm. The spectrometer was equipped with a Xe900 arc non ozone lamp 450 W (Steady State Lamp) and a R928P type detector (PMT detector). The excitation wavelength of 325 nm was used for all measurements; a width of excitation and emission slits was 0.3 nm.

2.11 Physisorption of Nitrogen

Specific surface area (SSA) of the samples was determined using the N_2 adsorption isotherms recorded at 77 K and calculated by means of the Brunauer, Emmett and Teller (BET) method using a 3Flex (Micromeritics Instruments, USA) apparatus after sample degassing at 150 °C for 24 h under less than 1 Pa vacuum. Adsorption–desorption isotherms were evaluated according to the BET theory for the p/p^0 range of 0.05–0.25.

2.12 Transmission Electron Microscopy

Transmission electron microscopy was performed with a JEOL 2100 microscope with LaB6 electron gun and an X-ray energy-dispersive spectrometer (EDS) as a detector. The accelerating voltage of 200 kV was applied. Micrographs were taken by a camera Tengra (EMSIS). Before analysis the samples were dispersed in ethanol and sonicated for 5 min. One drop of this solution was placed on a copper grid with a holey carbon film and dried at the room temperature.

2.13 Photoelectrochemical Measurement

Photoelectrochemical measurements were performed using a photoelectric spectrometer equipped with a 150 W xenon lamp, monochromator and potentiostat (Instytut Fotonowy, Poland) [41].

2.14 Photocatalytic Decomposition of AO7

Photocatalytic activity of the composites and pure $BiVO_4$ and g-C_3N_4 was tested using the azo-dye AO7. The photocatalytic decomposition was performed under irradiation of a Narva Black light blue lamp with the maximum intensity at 368 nm (36 W).

The photocatalytic procedure was described recently [42]. The 0.05 g of the powder sample was mixed with 150 ml of the AO7 solution (150 ml of the AO7 stock solution of 3×10^{-5} mol l^{-1}). The prepared suspension was stirred (400 rpm) for 30 min in dark and after 30 min an UV light was switched on. From the start of irradiation the suspension was sampled in periodic intervals. The suspension was sampled with a 5 ml syringe (2 ml of the suspension was taken) and filtered (syringe filter with 0.45 mm pore size). 1 ml of the filtered solution was diluted with demineralized water to 10 ml and absorbance was measured for this dilute solution. The AO7 absorbances were measured using a UV–VIS spectrometer Specord 250 Plus with software WinASPECT PLUS (version 4.1.0.0) in 1 cm quartz glass cuvettes at the absorption maximum of 483 nm.

2.15 Photocatalytic Decomposition of N₂O

The N_2O photocatalytic decomposition was conducted in a stainless steel batch photoreactor with an 8 W Hg lamp ($\lambda = 365$ nm) as a source of the irradiation. A photoreactor with the photocatalyst inside was purged with a N_2O/He mixture (N_2O concentration was 1050 ppm). The photocatalytic procedure was described recently [41]. The reproducibility of N_2O photocatalytic decomposition was checked by repeated tests in the interval of 0–22 h.

3 Results and Discussion

The structure, texture, optical and photocatalytic properties of the $BiVO_4$/g-C_3N_4 composites as well as pure $BiVO_4$ and g-C_3N_4 were studied by several instrumental methods. The structure was studied by X-ray diffraction, FTIR and Raman spectroscopy. The texture was investigated by TEM and the measurements of SSA. The photocatalytic properties were studied by means of the decomposition of AO7 and nitrous oxide. The observed results were also compared with measured photocurrents.

3.1 X-Ray Diffraction Analysis

The XRD patterns are shown in Fig. 1. Monoclinic $BiVO_4$ was the dominant phase in all the composites (ICDD PDF card No. 00-014-0688): the space group I2/a and lattice constants $a = 0.51950$ nm, $b = 1.17010$ nm, $c = 0.50920$ nm, α

Fig. 1 XRD patterns of g-C_3N_4, $BiVO_4$ and $BiVO_4$/g-C_3N_4
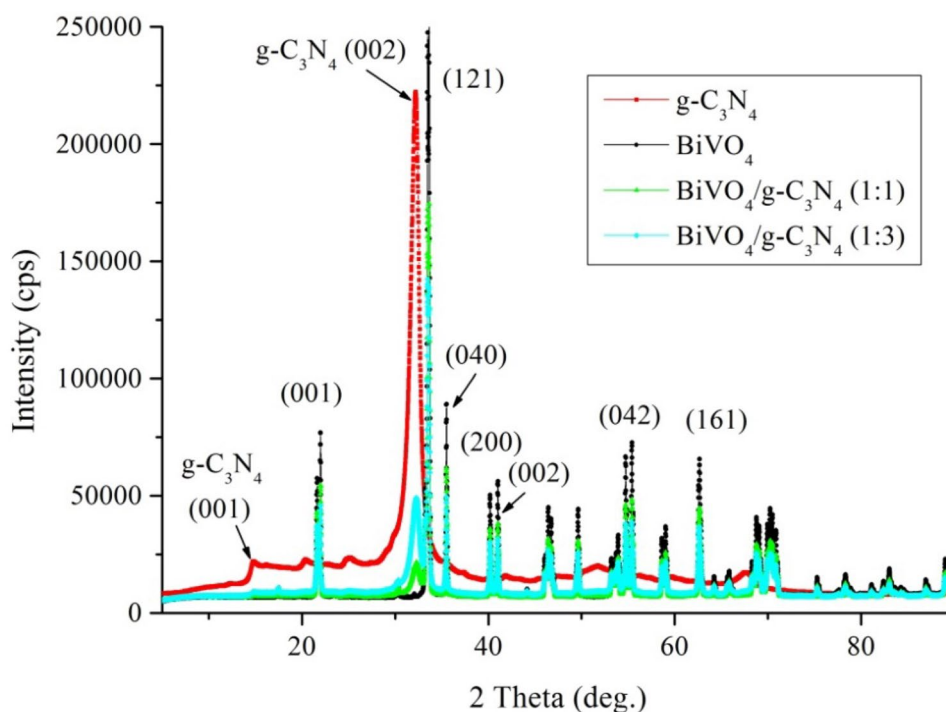
= γ = 90°, β = 90.38°. It was obtained from a precipitated tetragonal one [43, 44] and by heating at 500 °C.

The presence of g-C_3N_4 was confirmed by several weak and broad reflections, but the most typical are those around 14.9° and 32.2° 2theta. The first reflection at 14.9° 2theta ($d = 0.695$ nm) is indexed as the (100) plane and is attributed to in-plane tri-s-triazine units forming one-dimension melon strands. The second reflection at 32.2° 2theta ($d = 0.322$ nm) is interpreted as a long range interplanar stacking of aromatic systems with the (002) plane.

Refined lattice parameters and crystallite sizes are shown in Table 1. From the collected data, it was determined that the lattice parameters *a, b* and *c* of $BiVO_4$ were changed with the increasing content of g-C_3N_4. They slightly increased compared to pure $BiVO_4$ and $BiVO_4$ crystal matrix of the composites slightly expanded. It can be explained by the formation of a heterojunction between g-C_3N_4 and $BiVO_4$ structures. The crystallite sizes of $BiVO_4$ were calculated using Scherrer's formula as an average of three strongest diffractions at the (011), (121) and (040) planes. The other strong diffractions of the (042), (161) and (200) planes were also indicated in the XRD patterns [21, 26]. It is obvious that the crystallite sizes of $BiVO_4$ in the composites were significantly lower than that in pure $BiVO_4$ likely due to disintegration of large agglomerates into smaller particles by their connection with g-C_3N_4 ones. One of such agglomerates was examined by TEM as given below.

3.2 FTIR Spectrometry
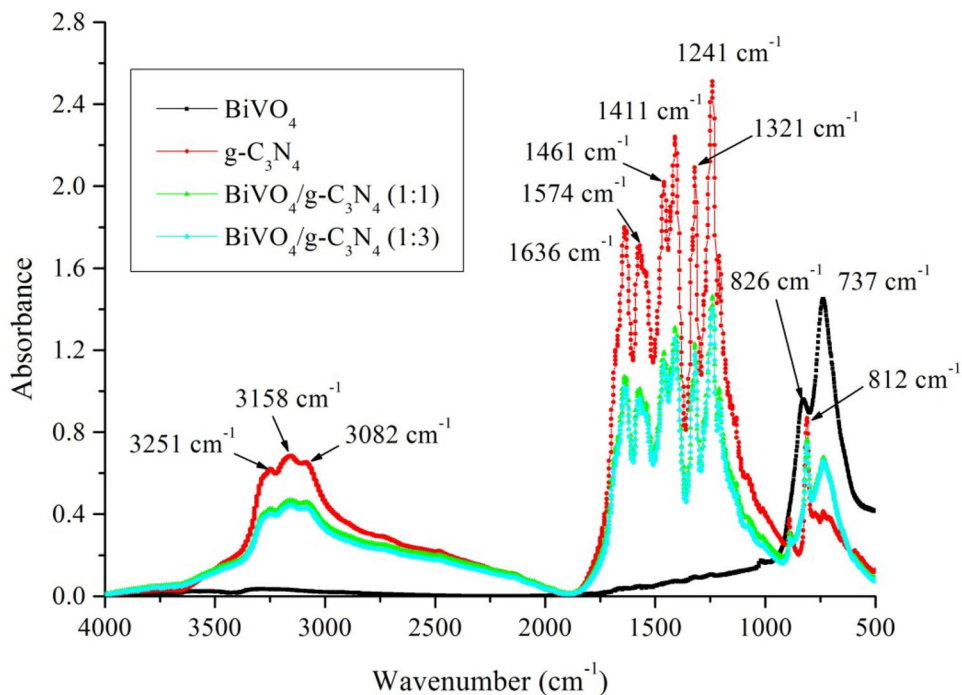
The $BiVO_4$/g-C_3N_4 composites were studied by FTIR spectrometry as shown in Fig. 2. The spectra of g-C_3N_4 contained the three broad spectral bands at 3251 cm^{-1}, 3158 cm^{-1}, and 3082 cm^{-1}, which can be attributed to the stretching vibrations of N–H bonds. Other significant bands can be observed at 1636 cm^{-1}, 1574 cm^{-1}, 1461 cm^{-1}, 1411 cm^{-1}, 1321 cm^{-1}, 1241 cm^{-1} and 812 cm^{-1}, which are typical for g-C_3N_4, e.g. [4, 45–47]. The strong bands between 1636 cm^{-1} and 1241 cm^{-1} correspond to the C=N and C–N bonds of heterocyclic rings. A medium band at 812 cm^{-1} can be attributed to the breathing mode of triazine units. Some bands typical for $BiVO_4$ were recorded at 737 cm^{-1} and 826 cm^{-1} which can be assigned to the antisymmetric stretching vibrations of V-O-V units [25, 26, 48].

Table 1 Structural properties of $BiVO_4$, g-C_3N_4 and their composites

Material	L (nm), g-C_3N_4	L (nm), $BiVO_4$	a (nm)	b (nm)	c (nm)
$BiVO_4$	–	240	0.51941	1.17016	0.50933
g-C_3N_4	9.6	–	–	–	–
$BiVO_4$/g-C_3N_4 (1:1)	12.0	192	0.51961	1.17064	0.50957
$BiVO_4$/g-C_3N_4 (1:3)	10.2	116	0.51971	1.17086	0.50968

Fig. 2 FTIR spectra of g-C_3N_4, $BiVO_4$ and $BiVO_4$/g-C_3N_4

3.3 Raman Spectrometry

The structure of BiVO4/g-C3N4 composites was also studied by the Raman spectrometry, see Fig. 3. The Raman spectra of $BiVO_4$ show a strong band at 815 cm^{-1} with the shoulders at 706 cm^{-1}, 341 cm^{-1} and 210 cm^{-1}. The band at 815 cm^{-1} can be assigned to the antisymmetric stretching of bridging of VOV units [28, 48] as already mentioned above. The shoulders were explained by the stretching modes of two different types of VO bonds [49]. The band at 341 cm^{-1}, the doublet at 328 cm^{-1} and 364 cm^{-1} and the band at 201 cm^{-1} indicate the bending vibrations of VO$_3$ units and the stretching ones of BiO bonds, respectively [27, 48, 49]. Some bands corresponding to g-C$_3$N$_4$ were observed at 1230 cm^{-1}, 768 cm^{-1}, 706 cm^{-1}, 473 and 487 cm^{-1} (a double band) and 212 cm^{-1}. The band at 1230 cm^{-1} was ascribed to the =C(sp^2) bending vibrations [50]. The bands at 768 cm^{-1} and 706 cm^{-1} could be ascribed to the ring breathing mode I and bending NCN and stretching CN vibrations, respectively. The bands at 473 cm^{-1} and 212 cm^{-1} correspond to the ring breathing mode II and stretching CN vibrations, respectively [51].

3.4 XPS Analysis

The $BiVO_4$/g-C$_3$N$_4$ composites showed typical C 1s and N 1s peaks demonstrated in Fig. 4. The C 1s spectrum shows mainly one carbon peak at the binding energy (BE) of

Fig. 3 Raman spectra of g-C$_3$N$_4$, BiVO$_4$ and BiVO$_4$/g-C$_3$N$_4$
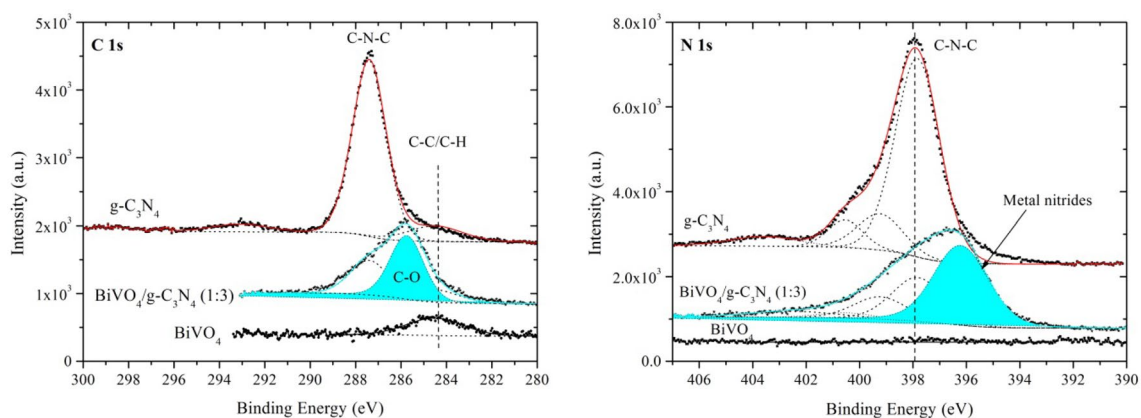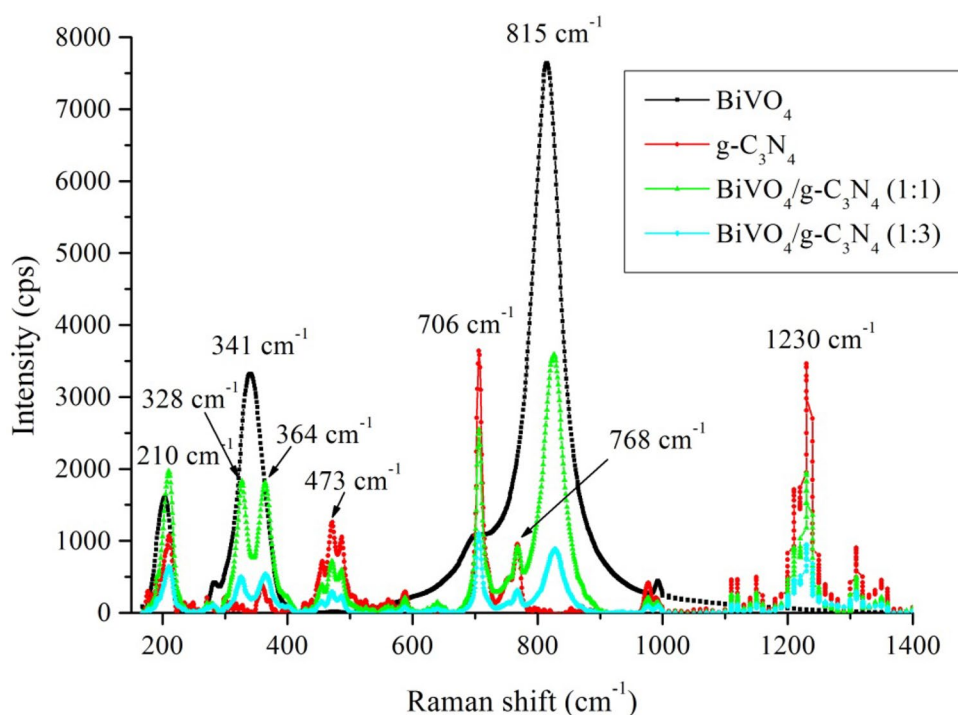
Fig. 4 High resolution XPS C 1s (left) and N 1s spectra of g-C$_3$N$_4$, BiVO$_4$ and BiVO$_4$/g-C$_3$N$_4$ (1:3) composite

287.4 eV corresponding to the C–N–C coordination with a small amount of C–C contamination at the BE of 284.5 eV (energy reference). In the N 1s spectrum (right Fig. 4) several binding energies can be found. The main peak shows the occurrence of C–N–C groups (397.8 eV) and tertiary nitrogen N–(C)$_3$ groups (399.2 eV). Deconvolution of the peaks also revealed a weak additional one at 400.5 eV which is indicative for amino groups. However, it is important to underline that the peak of tertiary amines is about four-times stronger than that of hydrogen bounds in amines. This proves a high degree of condensation beyond a linear melon structure which would possess no tertiary amines. The peak at 403.5 eV is attributed to charging effects. Integration of the C and N signals provided the atomic C/N ratio of 0.8 close to a theoretical one of 0.75 [52].

The BiVO$_4$/g-C$_3$N$_4$ composite (1:3) showed C 1s and N 1s peaks with the above given components and, additionally, there was a component at 285.7 eV representing C–O bonds in left Fig. 4 (the blue peak). Also, the presence of C=O bonds is probable but a corresponding peak was overlapped by the C–N–C one at 287.4 eV. Both C–O and C=O bonds confirm the formation of the heterojunction between BiVO$_4$ and g-C$_3$N$_4$. The N 1s peak was modified significantly. Although, all main components of g-C$_3$N$_4$ were confirmed there was a new dominant peak with the BE of 396.2 eV in which about 50% of N was involved, see the blue peak in right Fig. 5. This component should represent metal nitrides, such as bismuth and vanadium nitrides, in the composite. It indicates the formation of the heterojunction as well. In the literature, samples containing V and N are referred to show a N 1s main peak at 397.5 eV, a V 2p3/2 peak at 513.5 eV and an O 1s one at 531 eV [53]. The observed O 1s peak at 529.8 eV was supposed to indicate VO$_x$ systems [54]. The N 1s peak at 396.3 eV and the peak of V 2p3/2 at 512.3 eV were also referred in the literature [53]. The presence of C and N in pure BiVO$_4$ was negligible with the small C-C

component at 284.5 eV in the C 1s spectrum (energy reference). There was the main O 1s peak at 529.8 eV what is typical for OV [54] and also OBi bonds [55]. A small contribution of –OH groups at the BE of 533 eV was observed. These components were present in the BiVO$_4$/g-C$_3$N$_4$ composite as well.

The vanadium XPS spectra displayed in Fig. 5 are widely discussed in the literature [54, 56]. In pure BiVO$_4$ a wide peak of V 2p was observed and well fitted by a system of components V 2p3/2(IV) at 515.8 eV, V 2p3/2(V) at 517.2 eV, V 2p1/2(IV) at 523.2 eV and V 2p1/2(V) at 524.5 eV (spin split at 7.33 eV) proposed in [56]. Therefore, there is a mixture of vanadium IV and V oxidation states in the ratio of V(V)/V(IV) = 2. Since an achromatic X-ray source was used the fitting model also includes a main satellite of O 1s separated by 8.4 eV with intensity of 9.2% typical for achromatic sources.

The examined BiVO$_4$/g-C$_3$N$_4$ composites contained these components again but also the additional peaks observed at 519.4 eV and 526.6 eV are spin split at 7.2 eV as mentioned above. Those components cannot be vanadium nitrides [53], however, some similar components were observed in VO$_x$ thin films after intensive argon ions sputtering [54]. They could be related to some defect of the VO$_x$ structures. The spin split for vanadium oxides at 7.33 eV and at 7.5 eV for pure metal V were reported [54].

Bismuth in the BiVO$_4$ sample exhibited some core level peaks located at the BE of 159.0 eV and 164.3 eV which can be attributed to Bi 4f7/2 and Bi 4f5/2 orbitals, respectively, of a bismuth center in Bi$_2$O$_3$ [53]. A small broadening toward the lower BE was observed at 157 eV and 163.5 eV, which can be explained by the presence of metallic Bi–Bi bonds in amount of about 12% as a result of some defects in Bi–O–Bi structures of bismuth oxide. The BiVO$_4$/g-C$_3$N$_4$ composite exhibited a significant broadening of Bi 4f peaks toward the higher BE likely due to remaining Bi(NO$_3$)$_3$
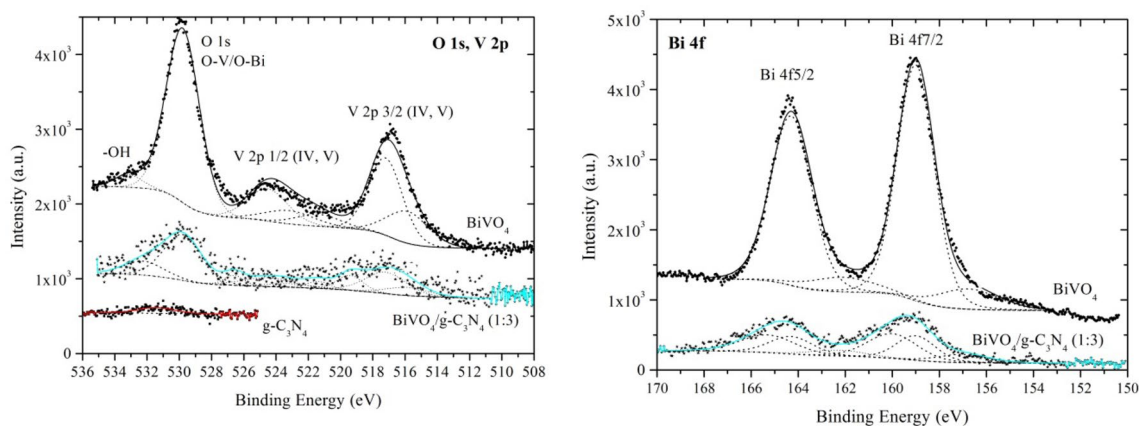
Fig. 5 High resolution XPS O 1s and V 2p spectra (left) and Bi 4f spectra of g-C$_3$N$_4$, BiVO$_4$ and BiVO$_4$/g-C$_3$N$_4$ (1:3)

impurities [55]. Therefore, it is highly probable a N 1s component presented in $BiVO_4$/g-C_3N_4 was related to the $Bi(NO_3)_3$ impurities as well.

3.5 TEM Analysis and SSA Measurements

The $BiVO_4$/g-C_3N_4 composites were studied by TEM as well. The micrographs of pure $BiVO_4$ and g-C_3N_4 are shown in Fig. 6a, b. Two micrographs and a EDS spectrum of $BiVO_4$/g-C_3N_4 (1:3) are shown in Fig. 6c–e, respectively. Large $BiVO_4$ particles with size of several hundred nanometres were observed. The TEM micrographs also show some bulk and exfoliated structures of g-C_3N_4. The EDS spectrum of $BiVO_4$/g-C_3N_4 confirmed the presence of both components.

SSA was measured by physisorption of nitrogen at 77 K and evaluated according to the BET isotherm. The SSA of $BiVO_4$ and g-C_3N_4 was determined at 6 $m^2\,g^{-1}$ and 35 $m^2\,g^{-1}$ and the SSA of $BiVO_4$/g-C_3N_4 (1:1) and $BiVO_4$/g-C_3N_4 (1:3) was determined at 23 $m^2\,g^{-1}$ and 28 $m^2\,g^{-1}$, respectively, as summarized in Table 2. It is obvious that by adding $BiVO_4$ to g-C_3N_4 the SSA of resulting composites decreased. In addition, the SSA of 35 $m^2\,g^{-1}$ of g-C_3N_4 was higher than that of bulk g-C_3N_4 and lower than that of exfoliated one [4, 57]. This means that g-C_3N_4 was partly exfoliated which was also observed by the TEM.

The real content of $BiVO_4$ in the prepared samples was determined at 100, 44 and 21 wt% for $BiVO_4$, $BiVO_4$/g-C_3N_4 (1:1) and $BiVO_4$/g-C_3N_4 (1:3), respectively (Table 2).

3.6 UV–Vis Diffuse Reflectance Spectrometry

UV–Vis DRS spectra were recorded for us to find the optical band gap energies of the $BiVO_4$/g-C_3N_4 composites as shown in Fig. 7. The reflectance values decreased with the decreasing content of g-C_3N_4. The spectra of pure g-C_3N_4 were composed from two bands corresponding to bulk and exfoliated g-C_3N_4 during the composites calcination which is also visible in the TEM micrographs (Fig. 6b, d). The composite spectra also contained these two bands of g-C_3N_4 and one band of $BiVO_4$. The optical band gap energies were evaluated by means of commonly employed Tauc's plot [58].

$$\varepsilon h\nu = C(h\nu - E_g)^p \qquad (3)$$

where ε is the molar extinction coefficient, $h\nu$ is the energy of incident photons, E_g is the optical band gap energy (hereinafter the band gap energy), C is the constant and p is the power depending on the type of electron transition: $p = 2$ and $p = 1/2$ are for direct and indirect semiconductors, respectively.

Based on the literature data, both $BiVO_4$ and g-C_3N_4 were evaluated supposing that to be direct semiconductors

[22, 26, 29, 40]. The E_g values of g-C_3N_4 were evaluated at 2.88 eV and 3.09 eV corresponding to bulk and exfoliated g-C_3N_4. All band gap energies are summarized in Table 2. In the composites, the E_g of bulk g-C_3N_4 was determined at 2.75 eV, 2.81 eV and 2.82 eV in accordance with the increasing content of g-C_3N_4. The E_g values related to exfoliated g-C_3N_4 varied in the narrow interval of 3.08–3.09 eV [4, 57] corresponding to electron transitions between highest occupied (HOMO) and lowest unoccupied (LUMO) molecular orbitals.

The E_g of $BiVO_4$ was determined at 2.51 eV in pure $BiVO_4$ and 2.46 eV and 2.43 eV in $BiVO_4$/g-C_3N_4 (1:1) and $BiVO_4$/g-C_3N_4 (1:3), respectively. These bad gap energies correspond to the transition of 6 s electrons of Bi to 3d orbitals of V in monoclinic $BiVO_4$. The light absorption of tetragonal $BiVO_4$ was due to the charge-transfer transitions between vanadium and oxygen in VO_4^{3-} and the corresponding E_g is about 2.9 eV [43, 44].

3.7 Photoluminescence Spectrometry

The photoluminescence spectra of g-C_3N_4, $BiVO_4$ and the $BiVO_4$/g-C_3N_4 composites were excited at the wavelength of 325 nm and are shown in Fig. 8. A broad band of g-C_3N_4 with a maximum at 470 nm can be explained by electron $\pi^* \rightarrow$ lone pair and $\pi^* \rightarrow \pi$ transitions [59]. The PL intensity decreased from pure g-C_3N_4 to pure $BiVO_4$ according to the decreasing portion of g-C_3N_4 in the composites. A partial splitting of one large band at 470 nm into two bands at 460 nm and 500 nm indicates the separation of photoinduced electron and holes *via* the heterojunction avoiding their recombination. The low PL intensity of $BiVO_4$ can be explained by the formation of structure defects working as electron traps as a result of the calcination. It was observed in the PL spectra of pure $BiVO_4$.

The PL spectra of pure $BiVO_4$ showed two bands at 450 and 500 nm, see Fig. S1 (Supplementary Materials). The first band can be ascribed to recombination of holes formed in the hybrid orbitals of Bi 6s and O 2p and electrons generated from V 3d orbitals [60]. The second one corresponds to recombination of electrons from the 3d orbitals of V with holes from the 6s orbitals of Bi as given above (Fig. 8).

3.8 Photoelectrochemical Measurement

The photocurrent generation at 365 nm was recorded for each material with longer times for opened and closed shutter. The lowest amounts of photoinduced electron and holes were detected in pure $BiVO_4$ and the composite containing the highest amount of $BiVO_4$–$BiVO_4$/g-C_3N_4 (1:1). The second composite and pure g-C_3N_4 showed the same photocurrent which was higher than that of pure $BiVO_4$.
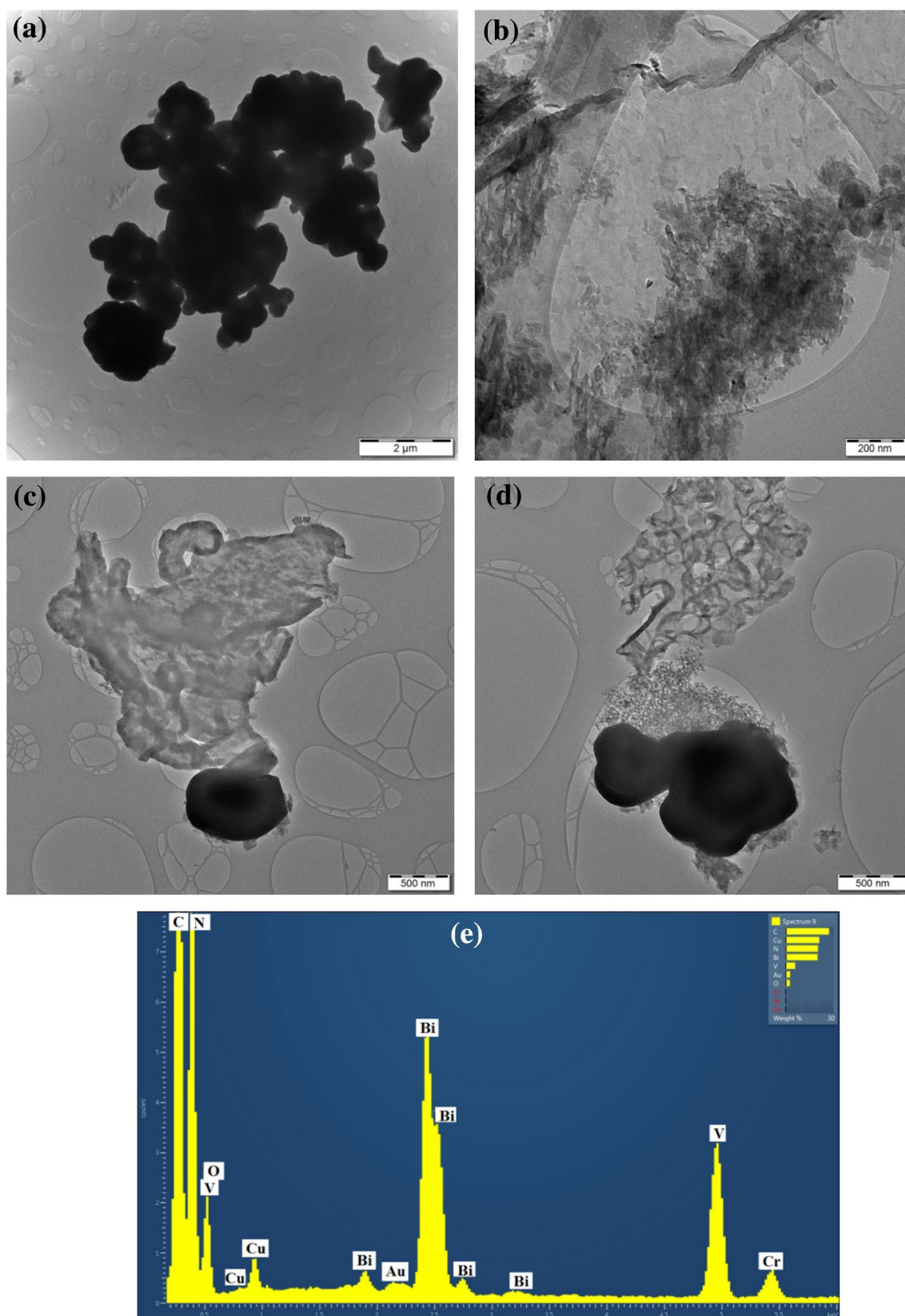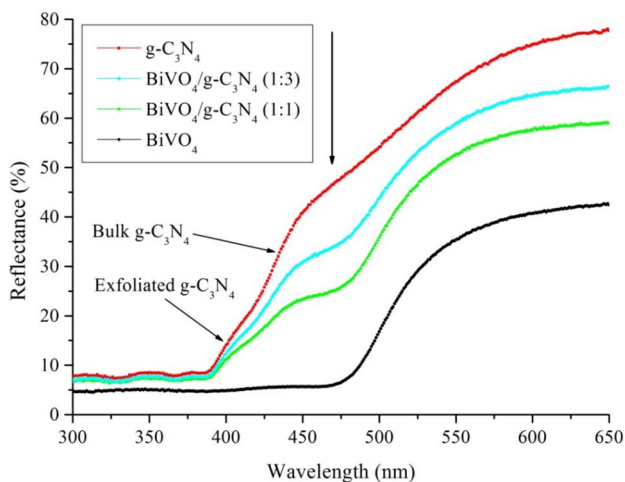
Fig. 6 TEM micrographs of BiVO4 (**a**), g-C3N4 (**b**) and BiVO4/g-C3N4 (1:3) (**c, d**), EDS spectrum of BiVO4/g-C3N4 (1:3) (**e**)

Table 2 Characteristics of g-C_3N_4, $BiVO_4$ and their composites

Sample	SSA (m^2 g^{-1})	Real content of $BiVO_4$ (wt%)	E_g bulk g-C_3N_4 (eV)	E_g $BiVO_4$ (eV)
$BiVO_4$	6	100	–	2.51
g-C_3N_4	35	0	2.88	–
$BiVO_4$/g-C_3N_4 (1:1)	23	44	2.75	2.46
$BiVO_4$/g-C_3N_4 (1:3)	28	21	2.82	2.43

Band gap energy of exfoliated g-C_3N_4 was 3.08–3.09 eV

Fig. 7 UV–Vis diffuse reflectance spectra of g-C_3N_4, $BiVO_4$ and $BiVO_4$/g-C_3N_4

3.9 BiVO$_4$/g-C$_3$N$_4$ Heterojunction Study

The band gap energies of $BiVO_4$ and g-C_3N_4 were used for the estimation of their band edge potentials according to empirical equations

$$E_{VB} = X - E^0 + 0.5E_g \tag{4}$$

$$E_{CB} = E_{VB} - E_g \tag{5}$$

where E_{VB} is the valence band (VB) edge potential, X is electronegativity of a semiconductor obtained as a geometric mean of constituent atoms, $E^0 = 4.5$ eV is the energy of free electrons vs vacuum, E_{CB} is the conduction band (CB) edge potential. The semiconductors' electronegativity $X = 4.67$ eV [24] for g-C_3N_4 and 6.04 eV for $BiVO_4$ [22, 29] were adopted from the literature. Taking into account the determined band gap energies of pure g-C_3N_4 and $BiVO_4$, their edge potentials were calculated as follows: $E_{VB} = 1.61$ eV and $E_{CB} = -1.27$ eV for g-C_3N_4 and $E_{VB} = 2.80$ eV and $E_{CB} = 0.29$ eV for $BiVO_4$; they are demonstrated in Fig. S2. The edge potentials were compared with the standard redox

Fig. 8 Photoluminescence spectra of g-C_3N_4, $BiVO_4$ and $BiVO_4$/g-C_3N_4 composites
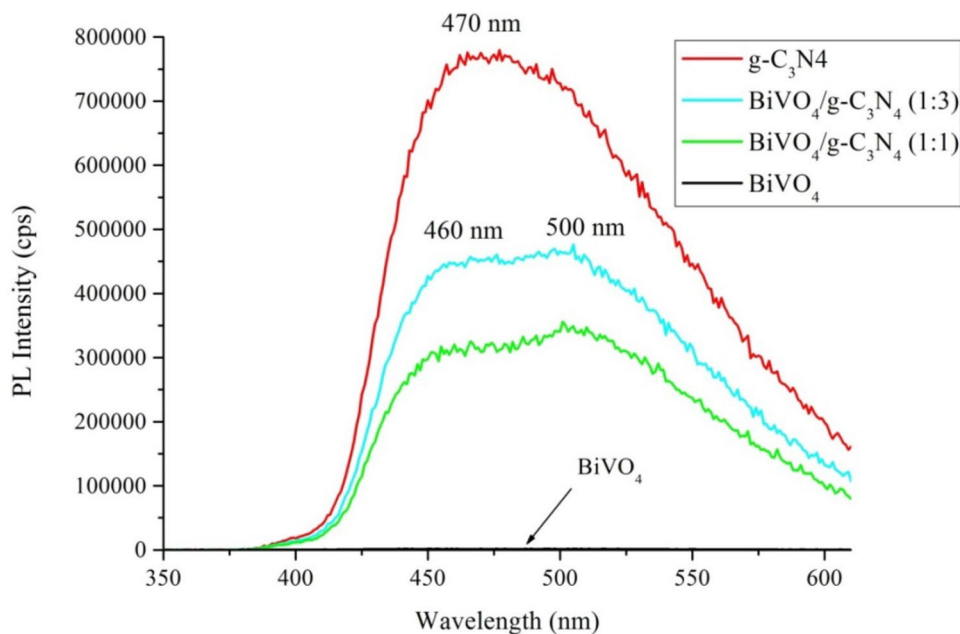
potentials of hydroxyl and superoxide radicals: $E^0(OH/H_2O) = 2.74$ V [61], $E^0(O_2/O_2^{\bullet-}) = -0.33$ V [61] and $E^0(OH–/OH\bullet) = 1.99$ V [62]. The redox potential of $E^0(O_2/O_2^{\bullet-}) = -0.16$ V was also referred for the concentration of 1 mol l^{-1} of O_2 [61].
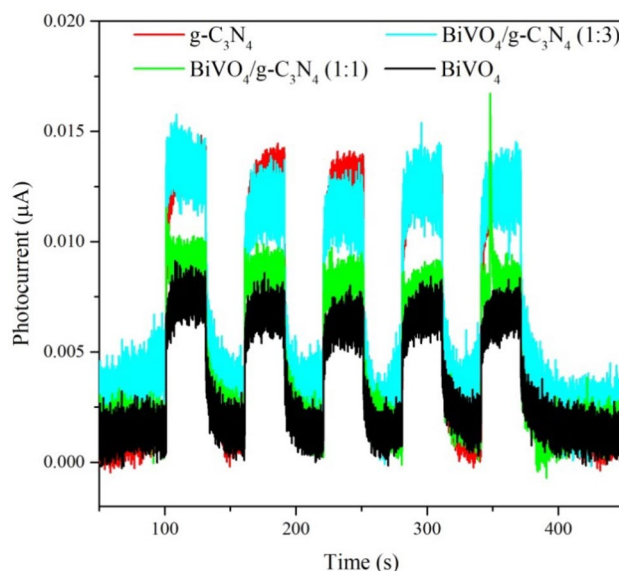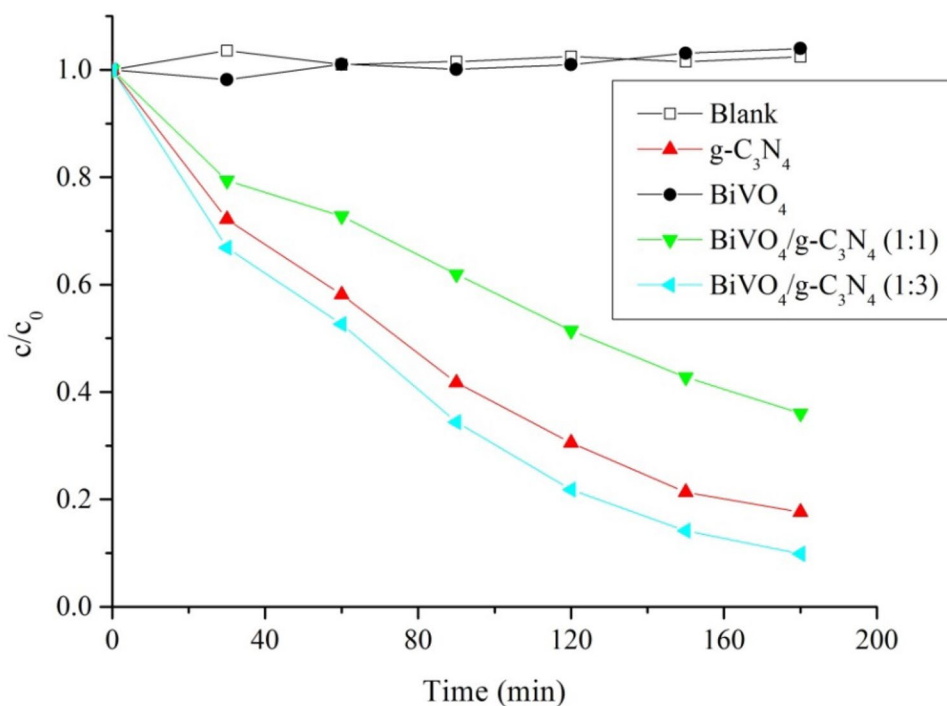
3.10 Photocatalytic Activity

3.10.1 Photocatalytic Decomposition of AO7

The photocatalytic activity of the composites and pure g-C_3N_4 and $BiVO_4$ was studied by means of the decomposition of AO7 under irradiation with the maximum intensity at 368 nm as shown in Fig. 9. Unlike the prepared materials (photocatalysts), AO7 absorbed the irradiation very little and, therefore, its sensitization was not supposed [63, 64]. The photocatalytic activity of $BiVO_4$ was negligible and similar to a blank solution with no photocatalyst. The activity of the other materials increased in the order $BiVO_4$/g-C_3N_4 (1:1) < g-C_3N_4 < $BiVO_4$/g-C_3N_4 (1:3). These results are in accordance with those of photoelectrochemical measurement (Fig. 10). The material with the smallest photocurrent response ($BiVO_4$) proved the smallest activity in the photooxidation reaction (the photocatalytic decomposition of AO7).

The very low activity of $BiVO_4$ was also observed by other authors [21, 22, 24, 30, 65] and was explained by particles morphology and size [30] and their negative surface charge [65]. In this case, a very likely reason is recombination of photoinduced electrons and holes in $BiVO_4$ defects

Fig. 10 Time based photocurrent response plots of g-C_3N_4, $BiVO_4$ and $BiVO_4$/g-C_3N_4 composites

[44] formed during the calcination which was documented by its low photoluminescence as already discussed. The heterojunction between $BiVO_4$ and g-C_3N_4 was supposed to facilitate the separation of electrons and holes and, thus, to increase the photocatalytic activity [21–24, 40].

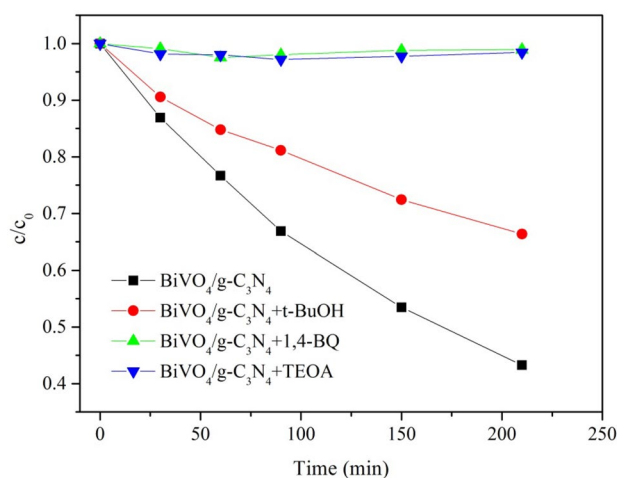Based on the calculated edge potentials of g-C_3N_4 and $BiVO_4$ the formation of hydroxyl radicals was assumed by the reactions of holes and electrons as follows

Fig. 9 Photocatalytic decomposition of AO7 using g-C_3N_4, $BiVO_4$ and $BiVO_4$/g-C_3N_4 composites

$$h^+ + H_2O \rightarrow OH^\bullet + H^+ \tag{6}$$

$$h^+ + OH^- \rightarrow OH^\bullet \tag{7}$$

$$e^- + O_2 \rightarrow O_2^{\bullet-} \tag{8}$$

$$O_2^{\bullet-} + H^+ \leftrightharpoons HO_2^\bullet \,(pK_a = 4.8) \tag{9}$$

$$2\,HO_2^\bullet \rightarrow H_2O_2 + O_2 \tag{10}$$

$$H_2O_2 + e^- \rightarrow OH^\bullet + OH^- \tag{11}$$
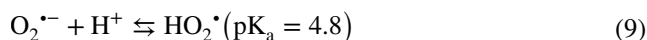
Since $BiVO_4$ was photocatalytically inactive, only g-C_3N_4 and $BiVO_4$/g-C_3N_4 (1:3) were examined for us to confirm the formation of superoxide and hydroxyl radicals and holes using some scavengers. For this purpose, the scavengers 1,4-BQ for superoxide radicals, t-BuOH for hydroxyl radicals and TEOA for holes were employed. The photocatalytic decomposition of AO7 in the presence of $BiVO_4$/g-C_3N_4 (1:3) and the scavengers is shown in Fig. 11. In all cases, the scavengers reduced (t-BuOH) or nearly inhibited (1,4-BQ and TEOA) the decomposition of AO7. It confirmed the formation of the radicals and holes according to Eqs. (6–11).

The CB of $BiVO_4$ is more positive than the standard redox potentials of the $O_2/O_2^{\bullet-}$ couple, therefore, from a view of thermodynamics electrons in this CB could not form the $O_2^{\bullet-}$ radicals [24]. The VB of $BiVO_4$ is more positive than the standard redox potentials of the $OH\bullet/H_2O$ and $OH^-/OH\bullet$ couples, thus, the holes in $BiVO_4$ were able to form the $OH\bullet$ radicals. However, the negligible photocatalytic activity and low luminescence of $BiVO_4$ were already explained by its defect structure.

Since the $O_2^{\bullet-}$ radical were formed in the presence of $BiVO_4$/g-C_3N_4 (1:3) a direct Z-scheme heterojunction [66] was only possible to be created during the composites

synthesis. Afterward, electrons from the CB of $BiVO_4$ recombined with holes in the VB of g-C_3N_4 and remaining charge carriers were able to take part in the photocatalytic reactions. The Z-scheme heterojunction in $BiVO_4$/g-C_3N_4 photocatalysts was also reported by Tian et al. [24]. On conditions that a type-II heterojunction between the conduction and valence bands of g-C_3N_4 and $BiVO_4$ was formed the redox potentials of both electrons and holes would be too low to take part in the reactions Eqs. (6–11).

3.11 Photocatalytic Decomposition of N_2O

The effect of irradiation time on the N_2O photocatalytic decomposition was probed in the presence of both the $BiVO_4$/g-C_3N_4 composites and pure $BiVO_4$ and g-C_3N_4 for the time period of 0–22 h. The time dependences of the N_2O conversion for photocatalysis and photolysis were depicted in Fig. 12. It is evident the conversion of nitrous oxide was increasing over the time. The photolysis led only to the 6% conversion of N_2O after 22 h of irradiation and each prepared material was found to be more effective. The highest N_2O conversion was observed in the presence of $BiVO_4$/g-C_3N_4 (1:3). On the other hand, pure $BiVO_4$ demonstrated the smallest photoactivity similarly as at the decomposition of AO7.

3.12 Comparison of Photocatalytic Reactions

As already mentioned, the photocatalytic activity of the prepared composites was investigated in two different reactions: (i) the photocatalytic decomposition of AO7 and (ii)

Fig. 11 Photocatalytic decomposition of AO7 in the presence of $BiVO_4$/g-C_3N_4 (1:3) and scavengers
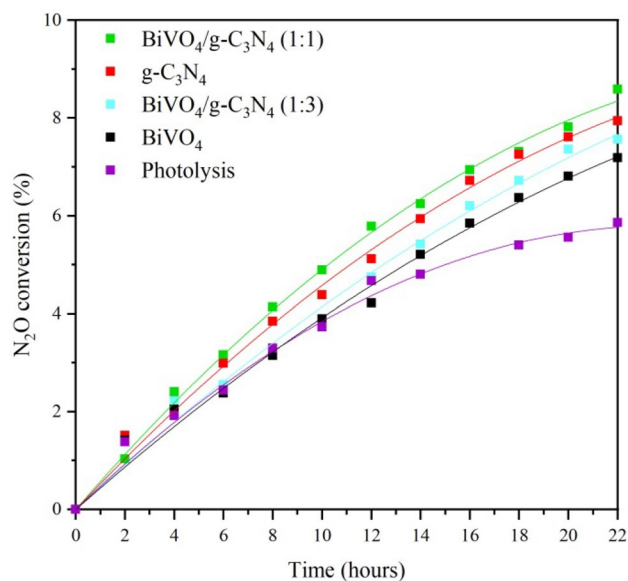
Fig. 12 The time dependence of N_2O conversion over prepared photocatalysts under UVA irradiation ($\lambda = 365$ nm)

the photocatalytic decomposition of N_2O. The photocatalytic decomposition of AO7, where a main role was played by photoinduced holes, can be marked as a photooxidation reaction. The first step of this photooxidation is the reaction of holes with water and the production of hydroxyl radicals which are one of the most powerful oxidizing agents. The mechanism and photoactivity of that reaction was described above.

In case of the N_2O photocatalytic decomposition, the most important species are photoinduced electrons. The reaction is started by electrons according the equation (Eq. 12) [67]:

$$N_2O + e^- \rightarrow N_2 + O^-_{ads} \tag{12}$$

The adsorbed oxygen on the photocatalyst's surface is oxidized by holes (Eq. 13) as

$$2O^-_{ads} + 2h^+ \rightarrow 2O_2 \tag{13}$$
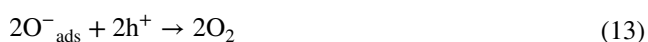
In general, the photocatalytic activity can be influenced by light-absorption ability, surface properties and photoinduced charge separation efficiency. The SSA of the prepared materials is summarized in Table 1 and the dependence between the SSA and the N_2O conversion is demonstrated in Fig. 13. These findings indicate that the SSA was not the crucial factor that determined the photocatalytic activity of the materials.

The PL spectra (Fig. 8) served for the investigation of separation efficiency of electron–hole pairs. The weaker PL intensities indicate the better separation of electrons and holes which can lead to their higher photocatalytic activity. As already mentioned, the decreasing PL intensity of the

Fig. 13 Dependence between the photocatalytic activity of the N_2O decomposition and SSA for different photocatalysts

composites can be explained by the lower content of g-C_3N_4 and also by supressing the recombination of photoinduced charge *via* the heterojunction between g-C_3N_4 with $BiVO_4$. In addition, the wide band splitting at 470 nm supports idea of the electron–holes separation. The smallest intensity of PL was observed at $BiVO_4/g$-C_3N_4 (1:1) which is in agreement with its highest activity of the photocatalytic decomposition of N_2O. The similar findings were observed by other authors [22, 68, 69].

It follows from the previous results that the Z-scheme heterojunction of $BiVO_4/g$-C_3N_4, which affected their properties, such as light absorption, crystal structure, specific surface area and charge carrier mobility, was successfully created. The formation of V^{4+} in the composites could increase mobility of electrons and holes. Furthermore, the V^{4+} produced oxygen vacancy acted as the centre of photocatalytic sites and chemisorbed species (Eq. 13) resulting in better photoelectrochemical properties. That hypothesis was confirmed by Safei et al. [70] who dealt with the photoelectrochemical performance of Z-scheme $BiVO_4/g$-C_3N_4 photocatalysts and supported with the experimental results of Density Functional Theory (DFT) simulations. The photoinduced electrons from the CB of g-C_3N_4 directly reduced nitrous oxide (Eq. 12) while the holes from the VB of $BiVO_4$ oxidized adsorbed oxygen coming from the decomposition of N_2O (Eq. 13). At the same time the electrons from the CB of $BiVO_4$ were recombining with the holes from the VB of g-C_3N_4.

4 Conclusion

The composites of $BiVO_4/g$-C_3N_4 were prepared by the calcination of mixed monoclinic $BiVO_4$ and bulk g-C_3N_4 at 300 °C for 4 h. During this process bulk g-C_3N_4 was partly exfoliated. The presence of both components was confirmed by the FTIR and Raman spectroscopy and TEM (EDS). The specific surface area was determined using the physisorption of nitrogen (the BET method) at 23–28 m^2 g^{-1} of the composites and 6 m^2 g^{-1} and 35 m^2 g^{-1} of pure $BiVO_4$ and g-C_3N_4, respectively.

The band gap energies were determined by Tauc's method at 2.42–2.46 eV of $BiVO_4$ and 2.75–2.82 eV and 3.08–3.06 of bulk and exfoliated g-C_3N_4, respectively. It means that both $BiVO_4$ and bulk g-C_3N_4 were able to absorb the visible irradiation. The band gap energies of the composites shifted due to the heterojunction between $BiVO_4$ and g-C_3N_4. It was confirmed by the XPS which identified the presence of C–O and C=O bonds and metal (bismuth and vanadium) nitrides in the composites. The existence of the heterojunction was also confirmed by the PL spectroscopy.

The photocatalytic activity of the composites was investigated by the decomposition of AO7 and nitrous oxide. The
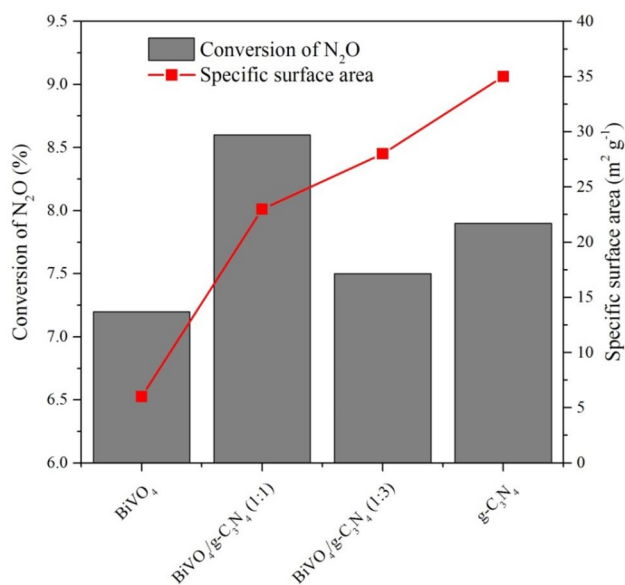
BiVO$_4$/g-C$_3$N$_4$ (1:3) composite was the most active one for the decomposition of AO7. The experiments with the scavengers 1,4-BQ, t-BuOH and TEOA proved that the AO7 decomposition was mainly performed by holes and following hydroxyl radicals which were formed only due to the direct Z-scheme heterojunction between both components. The different situation was observed in case of N$_2$O when the BiVO$_4$/g-C$_3$N$_4$ (1:1) composite was the most active photocatalyst and photoinduced electrons were the most important species.

The formation of the Z-scheme heterojunction between BiVO$_4$ and g-C$_3$N$_4$ creates a promising area for further research, especially in the field of environmental technologies. This study demonstrates suitability of the BiVO$_4$/g-C$_3$N$_4$ composites for the photocatalytic decomposition of risky environmental pollutants, such as the azo-dye AO7 and nitrous oxide. However, there are a lot of various harmful organic and inorganic compounds in the environment which could be removed by the photocatalytic decomposition as well. It will be the aim of our next research.

References

1. K.M. Yu, M.L. Cohen, E.E. Haller, W.L. Hansen, A.Y. Liu, I.C. Wu, Observation of crystalline C$_3$N$_4$. Phys. Rev. B **49**(7), 5034–5037 (1994). https://doi.org/10.1103/PhysRevB.49.5034

2. E. Kroke, Novel group 14 nitrides. Coord. Chem. Rev. **248**(5–6), 493–532 (2004). https://doi.org/10.1016/j.ccr.2004.02.001

3. X. Wang, K. Maeda, A. Thomas, K. Takanabe, G. Xin, J.M. Carlsson, K. Domen, M. Antonietti, A metal-free polymeric photocatalyst for hydrogen production from water under visible light. Nat. Mater. **8**(1), 76–80 (2009). https://doi.org/10.1038/nmat2317

4. P. Praus, L. Svoboda, M. Ritz, I. Troppová, M. Šihor, K. Kočí, Graphitic carbon nitride: synthesis, characterization and photocatalytic decomposition of nitrous oxide. Mater. Chem. Phys. **193**, 438–446 (2017). https://doi.org/10.1016/j.matchemphys.2017.03.008

5. G. Dong, Y. Zhang, Q. Pan, J. Qiu, A fantastic graphitic carbon nitride (g-C$_3$N$_4$) material: electronic structure, photocatalytic and photoelectronic properties. J. Photochem. Photobiol. C **20**, 33–50 (2014). https://doi.org/10.1016/j.jphotochemrev.2014.04.002

6. J. Wen, J. Xie, X. Chen, X. Li, A review on g-C$_3$N$_4$-based photocatalysts. Appl. Surf. Sci. **391**, 72–123 (2017). https://doi.org/10.1016/j.apsusc.2016.07.030

7. H. Li, L. Wang, Y. Liu, J. Lei, J. Zhang, Mesoporous graphitic carbon nitride materials: synthesis and modifications. Res. Chem. Intermed. **42**(5), 3979–3998 (2015). https://doi.org/10.1007/s11164-015-2294-9

8. L. Jiang, X. Yuan, Y. Pan, J. Liang, G. Zeng, Z. Wu, H. Wang, Doping of graphitic carbon nitride for photocatalysis: a reveiw. Appl. Catal. B **217**, 388–406 (2017). https://doi.org/10.1016/j.apcatb.2017.06.003

9. L. Wang, C. Wang, X. Hu, H. Xue, H. Pang, Metal/graphitic carbon nitride composites: synthesis, structures, and applications. Chemistry **11**(23), 3305–3328 (2016). https://doi.org/10.1002/asia.201601178

10. W.-J. Ong (2017) 2D/2D graphitic carbon nitride (g-C$_3$N$_4$) heterojunction nanocomposites for photocatalysis: why does face-to-face interface matter? Front. Mater. https://doi.org/10.3389/fmats.2017.00011

11. J. Fu, J. Yu, C. Jiang, B. Cheng, g-C$_3$N$_4$-based heterostructured photocatalysts. Adv. Energy Mater. **8**(3), 1701503 (2018). https://doi.org/10.1002/aenm.201701503

12. D. Masih, Y. Ma, S. Rohani, Graphitic C$_3$N$_4$ based noble-metal-free photocatalyst systems: a review. Appl. Catal. B **206**, 556–588 (2017). https://doi.org/10.1016/j.apcatb.2017.01.061

13. S. Cao, J. Low, J. Yu, M. Jaroniec, Polymeric photocatalysts based on graphitic carbon nitride. Adv. Mater. **27**(13), 2150–2176 (2015). https://doi.org/10.1002/adma.201500033

14. G. Mamba, A.K. Mishra, Graphitic carbon nitride (g-C$_3$N$_4$) nanocomposites: a new and exciting generation of visible light driven photocatalysts for environmental pollution remediation. Appl. Catal. B **198**, 347–377 (2016). https://doi.org/10.1016/j.apcatb.2016.05.052

15. S. Kumar, S. Karthikeyan, A. Lee, g-C$_3$N$_4$-based nanomaterials for visible light-driven photocatalysis. Catalysts **8**(2), 74 (2018). https://doi.org/10.3390/catal8020074

16. K. Kočí, M. Reli, I. Troppová, M. Šihor, J. Kupková, P. Kustrowski, P. Praus, Photocatalytic decomposition of N$_2$O over TiO$_2$/g-C$_3$N$_4$ photocatalysts heterojunction. Appl. Surf. Sci. **396**, 1685–1695 (2017). https://doi.org/10.1016/j.apsusc.2016.11.242

17. M. Reli, P. Huo, M. Sihor, N. Ambrozova, I. Troppova, L. Matejova, J. Lang, L. Svoboda, P. Kustrowski, M. Ritz, P. Praus, K. Koci, Novel TiO$_2$/C$_3$N$_4$ photocatalysts for photocatalytic reduction of CO$_2$ and for photocatalytic decomposition of N$_2$O. J. Phys. Chem. A **120**(43), 8564–8573 (2016). https://doi.org/10.1021/acs.jpca.6b07236

18. P. Praus, L. Svoboda, R. Dvorský, M. Reli, M. Kormunda, P. Mančík, Synthesis and properties of nanocomposites of WO$_3$ and exfoliated g-C$_3$N$_4$. Ceram. Int. **43**(16), 13581–13591 (2017). https://doi.org/10.1016/j.ceramint.2017.07.067

19. M. Reli, L. Svoboda, M. Šihor, I. Troppová, J. Pavlovský, P. Praus, K. Kočí, Photocatalytic decomposition of N$_2$O over g-C$_3$N4/WO$_3$ photocatalysts. Environ. Sci. Pollut. Res. (2017). https://doi.org/10.1007/s11356-017-0723-6

20. P. Praus, L. Svoboda, R. Dvorský, J.L. Faria, C.G. Silva, M. Reli, Nanocomposites of SnO$_2$ and g-C$_3$N$_4$: preparation, characterization and photocatalysis under visible LED irradiation. Ceram. Int. **44**(4), 3837–3846 (2018). https://doi.org/10.1016/j.ceramint.2017.11.170

21. J. Cheng, X. Yan, Q. Mo, B. Liu, J. Wang, X. Yang, L. Li, Facile synthesis of g-C$_3$N$_4$/BiVO$_4$ heterojunctions with enhanced visible light photocatalytic performance. Ceram. Int. **43**(1), 301–307 (2017). https://doi.org/10.1016/j.ceramint.2016.09.156

22. M. Ou, Q. Zhong, S. Zhang, Synthesis and characterization of g-C$_3$N$_4$/BiVO$_4$ composite photocatalysts with improved visible-light-driven photocatalytic performance. J. Sol–Gel. Sci. Technol. **72**(3), 443–454 (2014). https://doi.org/10.1007/s10971-014-3454-x

23. J. Zhang, F. Ren, M. Deng, Y. Wang, Enhanced visible-light photocatalytic activity of a g-C$_3$N$_4$/BiVO$_4$ nanocomposite: a first-principles study. Phys. Chem. Chem. Phys. **17**(15), 10218–10226 (2015). https://doi.org/10.1039/c4cp06089j

24. N. Tian, H. Huang, Y. He, Y. Guo, T. Zhang, Y. Zhang, Mediator-free direct Z-scheme photocatalytic system: BiVO4/g-C3N4 organic-inorganic hybrid photocatalyst with highly efficient visible-light-induced photocatalytic activity. Dalton Trans. **44**(9), 4297–4307 (2015). https://doi.org/10.1039/c4dt03905j

25. R. Venkatesan, S. Velumani, A. Kassiba, Mechanochemical synthesis of nanostructured BiVO4 and investigations of related features. Mater. Chem. Phys. **135**(2–3), 842–848 (2012). https://doi.org/10.1016/j.matchemphys.2012.05.068

26. A. Zhang, J. Zhang, Hydrothermal processing for obtaining of BiVO4 nanoparticles. Mater. Lett. **63**(22), 1939–1942 (2009). https://doi.org/10.1016/j.matlet.2009.06.013

27. S. Kunduz, G.S. Pozan Soylu, Highly active BiVO4 nanoparticles: the enhanced photocatalytic properties under natural sunlight for removal of phenol from wastewater. Sep. Purif. Technol. **141**, 221–228 (2015). https://doi.org/10.1016/j.seppur.2014.11.036

28. J. Liu, H. Wang, S. Wang, H. Yan, Hydrothermal preparation of BiVO4 powders. Mater. Sci. Eng. **104**(1–2), 36–39 (2003). https://doi.org/10.1016/s0921-5107(03)00264-2

29. H. Li, G. Liu, X. Duan, Monoclinic BiVO4 with regular morphologies: hydrothermal synthesis, characterization and photocatalytic properties. Mater. Chem. Phys. **115**(1), 9–13 (2009). https://doi.org/10.1016/j.matchemphys.2009.01.014

30. W. Ma, Z. Li, W. Liu, Hydrothermal preparation of BiVO4 photocatalyst with perforated hollow morphology and its performance on methylene blue degradation. Ceram. Int. **41**(3), 4340–4347 (2015). https://doi.org/10.1016/j.ceramint.2014.11.123

31. M. Shang, W. Wang, L. Zhou, S. Sun, W. Yin, Nanosized BiVO4 with high visible-light-induced photocatalytic activity: ultrasonic-assisted synthesis and protective effect of surfactant. J. Hazard. Mater. **172**(1), 338–344 (2009). https://doi.org/10.1016/j.jhazmat.2009.07.017

32. W. Yin, W. Wang, L. Zhou, S. Sun, L. Zhang, CTAB-assisted synthesis of monoclinic BiVO4 photocatalyst and its highly efficient degradation of organic dye under visible-light irradiation. J. Hazard. Mater. **173**(1–3), 194–199 (2010). https://doi.org/10.1016/j.jhazmat.2009.08.068

33. U.M. García-Pérez, S. Sepúlveda-Guzmán, A. Martínez-de la Cruz, Nanostructured BiVO4 photocatalysts synthesized via a polymer-assisted coprecipitation method and their photocatalytic properties under visible-light irradiation. Solid State Sci. **14**(3), 293–298 (2012). https://doi.org/10.1016/j.solidstatesciences.2011.12.008

34. S.S. Dunkle, R.J. Helmich, K.S. Suslick, BiVO4 as a visible-light photocatalyst prepared by ultrasonic spray pyrolysis. J. Phys. Chem. C **113**(28), 11980–11983 (2009). https://doi.org/10.1021/jp903757x

35. J. Pérez-Ramírez, F. Kapteijn, K. Schöffel, J.A. Moulijn, Formation and control of N2O in nitric acid production. Appl. Catal. B **44**(2), 117–151 (2003). https://doi.org/10.1016/s0926-3373(03)00026-2

36. K. Kočí, S. Krejčíková, O. Šolcová, L. Obalová, Photocatalytic decomposition of N2O on Ag-TiO2. Catal. Today **191**(1), 134–137 (2012). https://doi.org/10.1016/j.cattod.2012.01.021

37. S. Garcia-Segura, E. Brillas, Applied photoelectrocatalysis on the degradation of organic pollutants in wastewaters. J. Photochem. Photobiol. C **31**, 1–35 (2017). https://doi.org/10.1016/j.jphotochemrev.2017.01.005

38. B. Bethi, S.H. Sonawane, B.A. Bhanvase, S.P. Gumfekar, Nanomaterials-based advanced oxidation processes for wastewater treatment: a review. Chem. Eng. Process. **109**, 178–189 (2016). https://doi.org/10.1016/j.cep.2016.08.016

39. L. Ming, H. Yue, L. Xu, F. Chen, Hydrothermal synthesis of oxidized g-C3N4 and its regulation of photocatalytic activity. J. Mater. Chem. A **2**(45), 19145–19149 (2014). https://doi.org/10.1039/C4TA04041D

40. O. Man, Q. Zhong, J. Zhang, Synthesis and characterization of g-C3N4/BiVO4 composite photocatalysts with improved visible-light-driven photocatalytic performance. J. Sol–Gel. Sci. Technol. **72**(3), 443–454 (2014). https://doi.org/10.1007/s10971-014-3454-x)

41. I. Troppová, M. Šihor, M. Reli, M. Ritz, P. Praus, K. Kočí, Unconventionally prepared TiO2/g-C3N4 photocatalysts for photocatalytic decomposition of nitrous oxide. Appl. Surf. Sci. **430**, 335–347 (2018). https://doi.org/10.1016/j.apsusc.2017.06.299

42. J. Lang, L. Matějová, I. Troppová, L. Čapek, J. Endres, S. Daniš, Novel synthesis of $Zr_xTi_{1-x}O_n$ mixed oxides using titanyl sulphate and pressurized hot and supercritical fluids, and their photocatalytic comparison with sol-gel prepared equivalents. Mater. Res. Bull. **95**, 95–103 (2017). https://doi.org/10.1016/j.materresbull.2017.07.023

43. H. Fan, T. Jiang, H. Li, D. Wang, L. Wang, J. Zhai, D. He, P. Wang, T. Xie, Effect of BiVO4 crystalline phases on the photoinduced carriers behavior and photocatalytic activity. J. Phys. Chem. C **116**(3), 2425–2430 (2012). https://doi.org/10.1021/jp206798d

44. A. Kudo, K. Omori, H. Kato, A novel aqueous process for preparation of crystal form-controlled and highly crystalline BiVO4 powder from layered vanadates at room temperature and its photocatalytic and photophysical properties. J. Am. Chem. Soc. **121**(49), 11459–11467 (1999). https://doi.org/10.1021/ja992541y

45. P. Wu, J. Wang, J. Zhao, L. Guo, F.E. Osterloh, Structure defects in g-C3N4 limit visible light driven hydrogen evolution and photovoltage. J. Mater. Chem. A **2**(47), 20338–20344 (2014). https://doi.org/10.1039/c4ta04100c

46. I. Papailias, T. Giannakopoulou, N. Todorova, D. Demotikali, T. Vaimakis, C. Trapalis, Effect of processing temperature on structure and photocatalytic properties of g-C3N4. Appl. Surf. Sci. **358**, 278–286 (2015). https://doi.org/10.1016/j.apsusc.2015.08.097

47. T. Komatsu, The first synthesis and characterization of cyameluric high polymers. Macromol. Chem. Phys. **202**(1), 19–25 (2001).

48. R.L. Frost, K.L. Erickson, M.L. Weier, O. Carmody, Raman and infrared spectroscopy of selected vanadates. Spectrochim Acta A Mol Biomol Spectrosc **61**(5), 829–834 (2005). https://doi.org/10.1016/j.saa.2004.06.006

49. X. Meng, L. Zhang, H. Dai, Z. Zhao, R. Zhang, Y. Liu, Surfactant-assisted hydrothermal fabrication and visible-light-driven photocatalytic degradation of methylene blue over multiple morphological BiVO4 single-crystallites. Mater. Chem. Phys. **125**(1–2), 59–65 (2011). https://doi.org/10.1016/j.matchemphys.2010.08.071

50. J. Jiang, L. Ou-yang, L. Zhu, A. Zheng, J. Zou, X. Yi, H. Tang, Dependence of electronic structure of g-C3N4 on the layer number of its nanosheets: a study by Raman spectroscopy coupled with first-principles calculations. Carbon **80**, 213–221 (2014). https://doi.org/10.1016/j.carbon.2014.08.059

51. L. Stagi, D. Chiriu, C.M. Carbonaro, R. Corpino, P.C. Ricci, Structural and optical properties of carbon nitride polymorphs. Diam. Relat. Mater. **68**, 84–92 (2016). https://doi.org/10.1016/j.diamond.2016.06.009

52. A. Thomas, A. Fischer, F. Goettmann, M. Antonietti, J.-O. Müller, R. Schlögl, J.M. Carlsson, Graphitic carbon nitride materials: variation of structure and morphology and their use as metal-free catalysts. J. Mater. Chem. **18**(41), 4893 (2008). https://doi.org/10.1039/b800274f

53. A. Glaser, S. Surnev, F.P. Netzer, N. Fateh, G.A. Fontalvo, C. Mitterer, Oxidation of vanadium nitride and titanium nitride coatings. Surf. Sci. **601**(4), 1153–1159 (2007). https://doi.org/10.1016/j.susc.2006.12.010

54. G. Silversmit, D. Depla, H. Poelman, G.B. Marin, R. De Gryse, Determination of the V2p XPS binding energies for different vanadium oxidation states (V^{5+} to V^{0+}). J. Electron Spectrosc. Relat.

Phenom. **135**(2–3), 167–175 (2004). https://doi.org/10.1016/j.elspec.2004.03.004

55. E.A. Abdullah, A.H. Abdullah, Z. Zainal, M.Z. Hussein, T.K. Ban (2012) Synthesis and characterisation of Penta-Bismuth heptaoxide nitrate, $Bi_5O_7NO_3$, as a new adsorbent for methyl orange removal from an aqueous solution. e-J. Chem. 9 (4). https://doi.org/10.1155/2012/707853

56. M.C. Biesinger, L.W.M. Lau, A.R. Gerson, R.S.C. Smart, Resolving surface chemical states in XPS analysis of first row transition metals, oxides and hydroxides: Sc, Ti, V, Cu and Zn. Appl. Surf. Sci. **257**(3), 887–898 (2010). https://doi.org/10.1016/j.apsusc.2010.07.086

57. L. Svoboda, P. Praus, M.J. Lima, M.J. Sampaio, D. Matýsek, M. Ritz, R. Dvorský, J.L. Faria, C.G. Silva, Graphitic carbon nitride nanosheets as highly efficient photocatalysts for phenol degradation under high-power visible LED irradiation. Mater. Res. Bull. **100**, 322–332 (2018). https://doi.org/10.1016/j.materresbull.2017.12.049

58. J. Tauc, R. Grigorovici, A. Vancu, Optical properties and electronic structure of amorphous germanium. Phys. Status Solidi **15**(2), 627–637 (1966). https://doi.org/10.1002/pssb.19660150224

59. Y. Zhang, Q. Pan, G. Chai, M. Liang, G. Dong, Q. Zhang, J. Qiu, Synthesis and luminescence mechanism of multicolor-emitting g-C_3N_4 nanopowders by low temperature thermal condensation of melamine. Sci. Rep. **3**, 1943 (2013). https://doi.org/10.1038/srep01943

60. D.-K. Ma, M.-L. Guan, S.-S. Liu, Y.-Q. Zhang, C.-W. Zhang, Y.-X. He, S.-M. Huang, Controlled synthesis of olive-shaped $Bi_2S_3/BiVO_4$ microspheres through a limited chemical conversion route and enhanced visible-light-responding photocatalytic activity. Dalton Trans. **41**(18), 5581–5586 (2012). https://doi.org/10.1039/C2DT30099K

61. P.M. Wood, The potential diagram for oxygen at pH 7. Biochem. J. **253**(1), 287–289 (1988). https://doi.org/10.1042/bj2530287

62. K. Li, X. Zeng, S. Gao, L. Ma, Q. Wang, H. Xu, Z. Wang, B. Huang, Y. Dai, J. Lu, Ultrasonic-assisted pyrolyzation fabrication of reduced SnO_{2-x}/g-C_3N_4 heterojunctions: enhance photoelectrochemical and photocatalytic activity under visible LED light irradiation. Nano Res. **9**(7), 1969–1982 (2016). https://doi.org/10.1007/s12274-016-1088-8

63. M. Rochkind, S. Pasternak, Y. Paz, Using dyes for evaluating photocatalytic properties: a critical review. Molecules **20**(1), 88–110 (2014). https://doi.org/10.3390/molecules20010088

64. X. Chen, W. Wang, H. Xiao, C. Hong, F. Zhu, Y. Yao, Z. Xue, Accelerated TiO_2 photocatalytic degradation of Acid Orange 7 under visible light mediated by peroxymonosulfate. Chem. Eng. J. **193–194**, 290–295 (2012). https://doi.org/10.1016/j.cej.2012.04.033

65. N. Wetchakun, S. Chaiwichain, B. Inceesungvorn, K. Pingmuang, S. Phanichphant, A.I. Minett, J. Chen, $BiVO_4/CeO_2$ nanocomposites with high visible-light-induced photocatalytic activity. ACS Appl Mater Interfaces **4**(7), 3718–3723 (2012). https://doi.org/10.1021/am300812n

66. J. Low, C. Jiang, B. Cheng, S. Wageh, A.A. Al-Ghamdi, J. Yu, A review of direct Z-scheme photocatalysts. Small Methods **1**(5), 1700080 (2017). https://doi.org/10.1002/smtd.201700080

67. A. Kudo, H. Nagayoshi, Photocatalytic reduction of N_2O on metal-supported TiO_2 powder at room temperature in the presence of H_2O and CH_3OH vapor. Catal. Lett. **52**, 109–111 (1998)

68. Z. Zhang, M. Wang, W. Cui, H. Sui, Synthesis and characterization of a core–shell $BiVO_4@g$-C_3N_4 photo-catalyst with enhanced photocatalytic activity under visible light irradiation. RSC Adv. **7**(14), 8167–8177 (2017). https://doi.org/10.1039/c6ra27766g

69. M. Ou, Q. Zhong, S. Zhang, L. Yu, Ultrasound assisted synthesis of heterogeneous g-$C_3N_4/BiVO_4$ composites and their visible-light-induced photocatalytic oxidation of NO in gas phase. J. Alloy. Compd. **626**, 401–409 (2015). https://doi.org/10.1016/j.jallcom.2014.11.148

70. J. Safaei, H. Ullah, N.A. Mohamed, M.F. Mohamad Noh, M.F. Soh, A.A. Tahir, N. Ahmad Ludin, M.A. Ibrahim, W.N.R. Wan Isahak, M.A. Mat Teridi, Enhanced photoelectrochemical performance of Z-scheme g-$C_3N_4/BiVO_4$ photocatalyst. Appl. Catal. B **234**, 296–310 (2018). https://doi.org/10.1016/j.apcatb.2018.04.056